JOURNAL OF PROPULSION AND POWER
Vol. 18, No. 5, September–October 2002

Analysis of Dual-Mode Hydrocarbon Scramjet Operation at Mach 4–6.5

R. A. Baurle* and D. R. Eklund*
Taitech, Inc., Beavercreek, Ohio 45430

Reynolds averaged Navier–Stokes calculations have been performed for a U.S. Air Force Research Laboratory/Aerospace Propulsion Office scramjet combustor designed for Mach 4.0–6.5 flight. The combustor flowpath is unique in that it is entirely free of flow obstructions with fuel injection from wall-mounted injection ports and flameholding established by means of a recessed cavity. Calculations were performed at the minimum (Mach 4.0) and maximum (Mach 6.5) flight design conditions. The combustor operated in dual mode at the Mach 4.0 condition. The precombustion shock train formed a region of low-momentum/separated flow adjacent to the combustor side wall. This proved to be a primary source of flameholding, with the recessed cavity adding additional flameholding support. The flow was not thermally choked at the Mach 6.5 condition, resulting in very little upstream interaction. The mixing process at the Mach 4.0 flight condition was considerably more efficient than that seen at the Mach 6.5 condition, due primarily to the shock-induced flow distortion and larger residence time. Even with the reduced mixing levels predicted at the Mach 6.5 condition, the combustion efficiency was comparable to that achieved at the Mach 4.0 condition. The solutions obtained for dual-mode operation were particularly sensitive to choice of turbulence model and values specified for the turbulent Prandtl and Schmidt numbers. Overall, the solution sensitivity to grid resolution was small relative to the solution sensitivity to modeling uncertainties.

Introduction

THE current U.S. Air Force initiative supporting scramjet development is the hypersonic technologies (HyTech) program, established in 1995.[1] The immediate application of these technologies is aimed at high-speed air-launched missile development. Liquid hydrocarbon fuels are preferred for this application over hydrogen-based fuels due to their higher density (and corresponding reduced fuel tank volume) and considerations such as ease of handling and increased safety during military operations. As with other hypersonic programs, the primary obstacles in the design of these vehicles center around the technologies required for the development of the propulsion system.

Researchers at the U.S. Air Force Research Laboratory/Aerospace Propulsion Office (AFRL/PRA) have developed and tested a scramjet combustor flowpath based on wall-mounted fuel injection coupled with a cavity-based flameholder. The potential advantages of this configuration over other common fuel injection/flameholding strategies that introduce flow obstructions are considerable. The placement of physical obstructions in the combustor (such as ramps or struts) enhance mixing by providing streamwise vortices that "stretch" the fuel-to-air interface. These components, however, require cooling, a severe complexity in high-enthalpy flow. Moreover, a significant portion of the hypersonic missile flight profile is at a reduced engine thrust level during cruise, and any additional internal drag caused by flow obstructions can result in substantial engine performance losses. In part because of these considerations, researchers at AFRL/PRA have focused their efforts on the use of nonintrusive fuel injectors combined with recessed cavity flameholders. All tests have been conducted at the supersonic combustion facility located at AFRL/PRA. This facility is presently capable of simulating flight Mach numbers between 4 and 8, peak stagnation conditions of 5 MPa and 2200 K, and air mass flow rates of up to 13.6 kg/s. A detailed discussion of the facility may be found in Ref. 2. The variable-geometry heat-sink combustor described in Ref. 2 has recently been replaced with a fixed-geometry water-cooled combustor. The entire rig is now water cooled, permitting longer test times that allow the wall temperature (heat flux) to reach true steady-state conditions.

The prediction of scramjet operation at low hypersonic flight Mach numbers ($4 \leq \text{Mach} \leq 7$) has proven to be a daunting task.[3–5] Combustor operation at these Mach numbers is typically dual mode, so that the heat release due to combustion forces a precombustion shock train upstream of the combustor. The shock system transitions the flow from supersonic to subsonic conditions within the nearly constant area duct (isolator) that separates the inlet from the combustor. The heat release due to combustion eventually expands the flow back to sonic conditions (thermally choked condition), and the combustor area divergence continues the expansion to supersonic conditions. The feedback mechanism between the precombustion shock train and downstream combustion zone is quite sensitive to small disturbances in the flowfield, requiring the use of state-of-the-art turbulence and combustion models. Moreover, the mixed supersonic and subsonic regions of the combustor require large sections of the flow to be solved simultaneously, forcing the use of efficient parallel algorithms and solution methodologies.

Pretest Reynolds averaged Navier–Stokes simulations have been performed for the AFRL/PRA water-cooled combustor rig at true Mach 4.0 and Mach 6.5 flight enthalpies. Calculations were also performed at conditions that closely approximate those used in tests of a similar heat-sink combustor described in earlier reports.[2,3,6] These conditions do not precisely match a particular flight condition. Instead, measurements at these conditions were used to calibrate numerical model constants (turbulent Schmidt and Prandtl numbers) and to determine the level of grid resolution required to capture the relevant time-averaged dual-mode flow physics.

Combustor Configuration

A schematic of the combustor rig flowpath considered in this investigation is shown in Fig. 1. The test rig consists of an interchangeable water-cooled facility nozzle, two removable water-cooled isolator sections, and a water-cooled fixed-geometry combustor. An uncooled partial nozzle is used to transition the combustor exit geometry to the calorimeter section. Vitiated air is supplied to the facility nozzle, providing high-enthalpy conditions for a variety of

Presented as Paper 2001-3299 at the AIAA/ASME/SAE/ASEE 37th Joint Propulsion Conference, Salt Lake City, UT, 8–11 July 2001; received 21 January 2002; revision received 24 April 2002; accepted for publication 20 May 2002.

*Senior Research Scientist, Computational Fluid Dynamics Group. Senior Member AIAA.

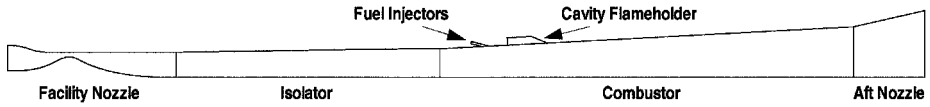

Fig. 1 Schematic of facility flowpath.

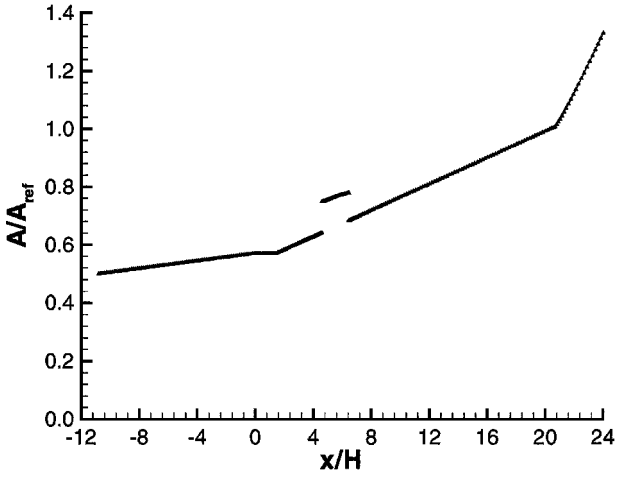

Fig. 2 Area distribution of isolator and combustor.

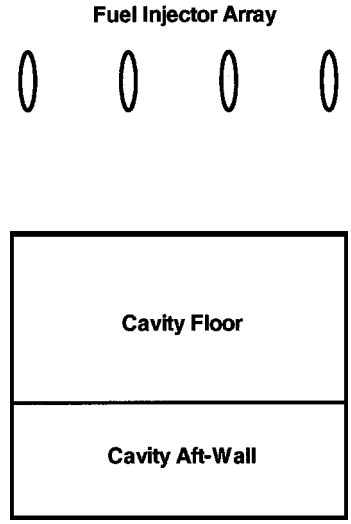

Fig. 3 Fuel injector arrangement relative to the cavity flameholder (flow direction is top to bottom).

simulated flight Mach numbers. Each facility nozzle is instrumented with an array of static pressure taps along the side wall, and each isolator section is instrumented with 60 pressure taps along the upper and lower walls. The combustor top, bottom, and side walls are instrumented with nearly 200 static pressure taps. All four walls of the combustor have removable inserts allowing optical access and/or installation of additional instrumentation. The cross-sectional area distribution from the isolator entrance to combustor exit is given in Fig. 2. The total area ratio is 2.014. The "body-side" wall of the isolator has a 0.75-deg divergence angle. The combustor has a small constant area section upstream of fuel injection, followed by a 2.6-deg divergence angle on the body-side surface. Further details of the test facility may be found in Ref. 2.

A plan-form view of the fuel injector/flameholder arrangement is shown in Fig. 3. This design consists of four low-angle (15 deg relative to the combustor surface) flush wall injectors upstream of a recessed cavity. The aft wall of the recessed cavity is angled (22.5 deg relative to the cavity floor) to provide relief from the self-sustained pressure oscillations associated with recessed cavity flows. All four injectors are fed from a common manifold, and each injector has its own static pressure tap to ensure that proper fuel conditions are being simulated. The injector block was designed to permit geometrical variations in cavity length-to-depth ratio, cavity aft wall angle, and distance downstream of fuel injection. Several ports are available along the bottom wall of the cavity for ignition sources, pressure taps, thermocouples, gas sampling devices, and fuel/air injection.

Modeling Approach

All computational results were obtained using the VULCAN Navier–Stokes code.[†] The numerical algorithms and physical models available in this code are quite representative of the class of solvers typically used for high-speed reacting flow computations. The code solves the Reynolds averaged conservation equations appropriate for calorically or thermally perfect gases with a cell-centered finite volume scheme. A variety of one-equation and two-equation turbulence models are available to describe the turbulent velocity field. Chemical reactions are accounted for with finite rate kinetics models based on the law of mass action. The code also contains full multigrid capabilities, allowing rapid convergence for steady-state problems. Recent additions to the code include arbitrary block to block non-C(0) continuous connectivity and block level parallelization using a message passing interface. These recent enhancements have greatly reduced the turnaround times required for dual-mode flowfield calculations. Further details describing the code may be found in Ref. 7.

All calculations were performed using the low-diffusion flux split scheme of Edwards.[8] The MUSCL parameter κ was chosen as one-third to minimize truncation error and the Van Leer flux limiter was employed to enforce total variation diminishing. The steady-state solutions were advanced in time using a diagonalized approximate factorization scheme. These solutions were advanced in time with a Courant–Friedrechs–Lewy number in the range of 1.5–2.5. Steady-state solutions could not be found for some of the simulations considered in this effort. In these instances, the time integration was performed in a time-accurate manner with a constant time step of 2.5 μs. In each time-accurate simulation, the unsteady behavior of the flow was strictly periodic, a common feature when using diffusive eddy-viscosity-based turbulence models. The observed periodic behavior allowed the extraction of an effective steady-state solution through an ensemble average of the flowfield during one cycle of the oscillation. A less diffusive simulation procedure, for example, large-eddy simulation, would result in a chaotic unsteady behavior, requiring a much larger time history to extract relevant flow statistics.

The turbulence models chosen for this work were the Menter baseline (BSL) and Menter shear stress transport (SST) models.[9] The BSL version of the Menter model is essentially the standard high Reynolds number Wilcox k–ω model near solid surfaces and smoothly switches to the standard Jones–Launder k–ϵ model near the outer portion of the boundary layer and in regions of free shear. This model attempts to take advantage of the robustness and accuracy of the k–ω formulation for wall-bounded flows, while retaining the somewhat more accurate k–ϵ formulation for free shear flows. The SST extension of this model addresses the tendency of most two-equation turbulence models to underpredict the level of separation for flows with adverse pressure gradient. This model accounts for the transport effects of the principal turbulent shear stress by limiting the eddy viscosity. To relax the grid requirements near solid surfaces, the wall-matching procedure developed by Wilcox[10] was used for all calculations. The compressibility correction of Wilcox[11] was also employed to account for the reduced mixing levels associated with high convective Mach numbers.

All calculations employed constant values for the turbulent Prandtl Pr_t and Schmidt Sc_t numbers, which control the turbulent

[†]Data available online at http://vulcan.cfd.larc.nasa.gov/jawhite/.

transport of energy and mass, respectively. Previous dual-mode calculations for a similar combustor[5] showed a high sensitivity to values specified for these parameters (particularly the Schmidt number), so a sensitivity study was repeated for the configuration analyzed in this work. The baseline values for the turbulent Prandtl and Schmidt numbers were chosen as 0.89 and 0.5, respectively. Other turbulent Schmidt numbers in the range of $0.25 \leq Sc_t \leq 0.75$ were considered with Pr_t fixed at 0.89. The turbulent Prandtl number was also varied ($0.45 \leq Sc_t \leq 1.8$) with the Sc_t fixed at 0.5.

Chemical kinetics were modeled as finite rate using a 3-step, 6-species reduced ethylene mechanism developed by Mawid (private communication) (see Table 1). Following Eklund et al.,[5] rate adjustments were made to this model to account for the presence of hydroxyl in the vitiated freestream. Hydroxyl has been found to reduce the ignition delay considerably even at concentration levels less than 1 ppm. The reduced model used in this work does not account for the presence of OH. Other reduced models for ethylene[12] allow for the presence of OH, but only in the context of the H_2–O_2 kinetic process that occurs after the ethylene fuel has been decomposed. In the detailed kinetic mechanism,[13] the effect of OH on ethylene ignition occurs predominantly through the initial H-abstraction reaction:

$$C_2H_4 + OH \rightleftharpoons C_2H_3 + H_2O$$

and the subsequent generation of the radical pool. Therefore, many of the reduced models that allow for the presence of OH can not properly account for the reduced ignition delay. The adjustment to the reaction rates is obtained by first assuming the flow to be in chemical equilibrium at the entrance of the facility nozzle. A finite rate (quasi-one-dimensional) calculation is then performed using the detailed kinetic mechanism through the facility nozzle to determine an estimate for the hydroxyl levels entering the combustor. The nozzle exit composition is then used as the initial composition for an ignition delay study. Finally, a comparison of ignition delay with the detailed kinetic mechanism and the reduced mechanism (over a range of expected combustor conditions) is performed to determine the rate adjustment. A detailed description of this procedure is outlined in Ref. 5.

Table 1 Model: 3-step, 6-species ethylene kinetic

Reaction	A^a	b	T_a, K
$C_2H_4 + O_2 \rightleftharpoons 2CO + 2H_2$	$2.10E{+}14$	0.0	18015.3
$2CO + O_2 \rightleftharpoons 2CO_2$	$3.48E{+}11$	2.0	10134.9
$2H_2 + O_2 \rightleftharpoons 2H_2O$	$3.00E{+}20$	−1.0	0.0

[a]Units are a multiple of $cm^3/mole \cdot s$.

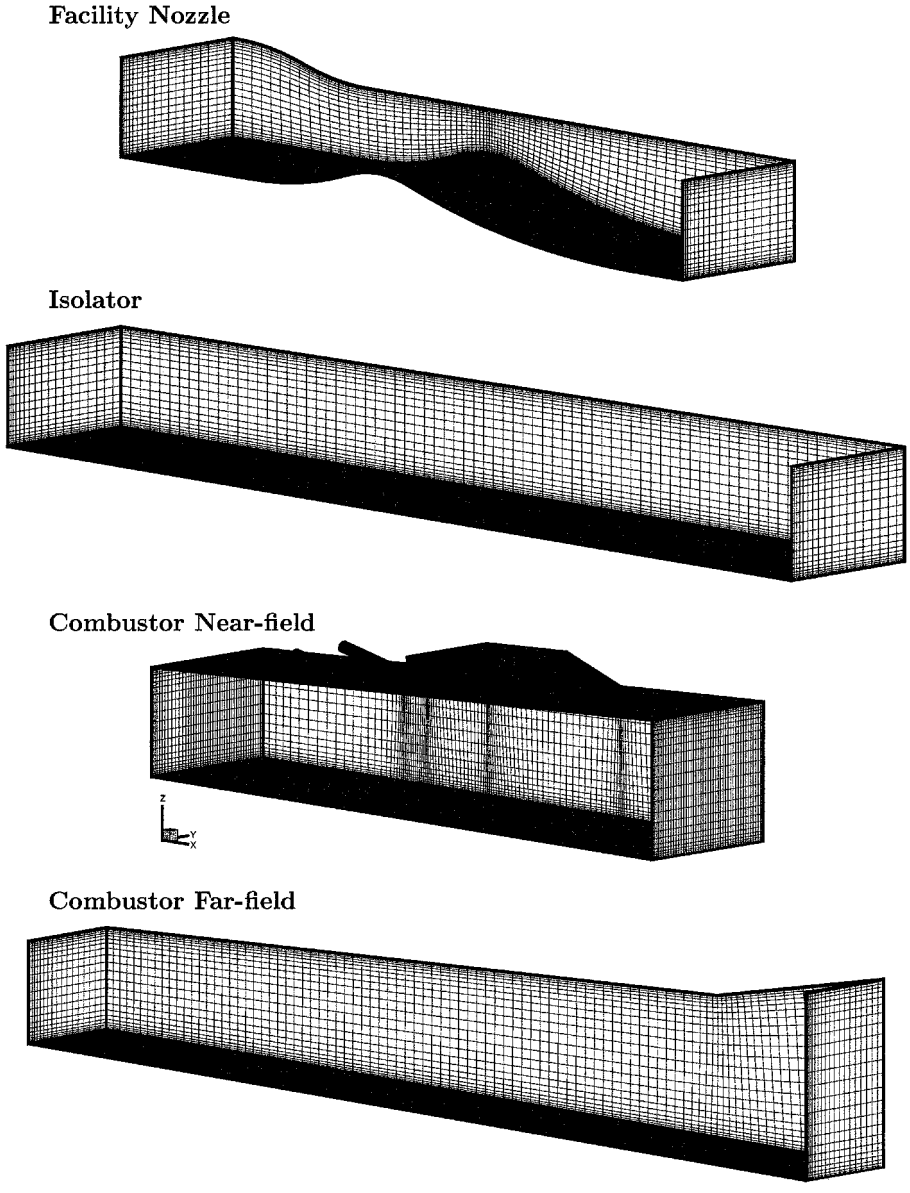

Fig. 4 Computational grid with every other grid point removed for clarity [non-C(0) patches present at the combustor near-field inflow and outflow planes].

Test Conditions and Grid Details

The computational domain for all simulations extended from the facility nozzle plenum to the exit of the partial nozzle (entrance of the calorimeter section). This computational domain, however, was broken up into separate regions wherever possible to reduce the computational costs. The subsonic portion of the facility nozzle and a small region downstream of the nozzle throat were solved as a separate domain. The remaining supersonic section of the nozzle was solved using an efficient space-marching algorithm. Cold-flow simulations allowed the isolator sections and far-field region of the combustor to be solved using the space-marching procedure as well, with an elliptical algorithm used only in the immediate vicinity of the cavity flameholder and fuel injection sites. Most reacting simulations, however, required that the entire isolator and combustor be solved as one entity with the fully elliptic algorithm due to large regions of subsonic/separated flow resulting from precombustion shock trains.

The grid generated for this computational domain consisted of 2.35×10^6 cells. Roughly 2×10^6 cells were placed in the isolator and combustor, with the remaining cells placed in the facility nozzle. Grid zones were generated for the interior of all fuel injector ports, which were integrated into the solution domain. This practice obviates the need for ad hoc profiles at the combustor/injector interface. The grid was clustered to all solid surfaces at a level appropriate for the use of wall functions ($y^+ \leq 50$). The grid was also clustered near the fuel injection ports and at the leading and trailing edges of the cavity flameholder. The grid generated for each facility component is shown in Fig. 4. The grid was broken up into a total of 22 grid zones. The 17 grid zones that comprised the isolator and combustor sections yielded good load balance statistics for use with either 3, 5, or 9 processors. The ideal speed up, defined as

$$\text{ideal speed up} \equiv \frac{\text{total cell count}}{\text{cell count of largest zone}} \tag{1}$$

was 2.98, 4.91, and 8.7 using 3, 5, and 9 processors, respectively. Two non-C(0) patches that is, nonaligned grid zone interfaces, were employed to remove unnecessary grid points in regions upstream and downstream of the fuel injection sites. These patches removed roughly 50% of the spanwise grid points required to resolve the injector near field. A secondary benefit of non-C(0) patches was that they permitted nearly isotropic cells in the core flow region of the isolator, providing a more efficient grid structure for wave propagation.

The nozzle inflow conditions were prescribed with a subsonic boundary condition that maintained constant plenum stagnation conditions. This boundary condition ensures that the desired mass flow rate (with allowances for boundary-layer growth) is achieved through the facility nozzle. The inflow conditions for the fuel injection ports were set in the same manner, allowing the injectant mass flow rate to adjust based on local conditions within the combustor. The combustor static pressure to injectant total pressure did not exceed the critical pressure ratio in any of the simulations performed in this effort; hence, the injector ports operated under choked conditions. The conditions for each case simulated are given in Tables 2–4. The vitiated inflow composition given in Tables 2–4 was obtained based on an assumption of complete reaction within the vitiator. A zero-gradient condition was applied at the combustor outflow plane, and flow symmetry was assumed at the spanwise centerplane of the combustor rig. The nozzle and isolator surfaces were defined as no-slip isothermal surfaces. The surface temperature was determined iteratively by comparing the computed total heat loss with the measured values. Heat loss data were not available for the water-cooled combustor section, so an adiabatic no-slip condition was applied to all combustor surfaces. This approximation was partially realized in the combustor rig by the application of a thermal barrier coating to all water-cooled combustor surfaces. The thermal barrier coating consisted of a nickel–chromium coating, followed by a 50–50 (by weight) nickel–chromium/zirconia coating, followed by a top coat of zirconia. The coating permits higher interior surface temperatures and reduces the cooling requirements of the water channels.

Table 2 Combustor conditions (M1.8 facility nozzle)

Nominal combustor conditions	Inflow	Fuel
Mach number	1.8	1.0
Total temperature, K	1187.0	300.0
Total pressure, kPa	574.5	1025.0
Equivalence ratio	——	0.715
C_2H_4 mass fraction	0.0	1.0
O_2 mass fraction	0.2313	0.0
N_2 mass fraction	0.6601	0.0
H_2O mass fraction	0.0303	0.0
CO_2 mass fraction	0.0783	0.0

Table 3 Combustor conditions (M2.2 facility nozzle)

Nominal combustor conditions	Inflow	Fuel
Mach number	2.2	1.0
Total temperature, K	902.2	425.0
Total pressure, kPa	689.5	1645.9
Equivalence ratio	——	1.0
C_2H_4 mass fraction	0.0	1.0
O_2 mass fraction	0.2314	0.0
N_2 mass fraction	0.7117	0.0
H_2O mass fraction	0.0159	0.0
CO_2 mass fraction	0.0410	0.0

Table 4 Combustor conditions (M3.0 facility nozzle)

Nominal combustor conditions	Inflow	Fuel
Mach number	3.0	1.0
Total temperature, K	1826.7	425.0
Total pressure, kPa	2633.8	1692.4
Equivalence ratio	——	1.0
C_2H_4 mass fraction	0.0	1.0
O_2 mass fraction	0.2283	0.0
N_2 mass fraction	0.5885	0.0
H_2O mass fraction	0.0511	0.0
CO_2 mass fraction	0.1321	0.0

Simulation Details and Convergence

All simulations were initiated on coarse grids (cell count reduction was a factor of either 8 or 64) to allow a rapid means of initializing the reacting flowfield. First, a cold-flow (mixing-only) solution was obtained on the coarsest grid considered. Ignition was then achieved by invoking a modified version of the kinetic model, where the Arrhenius activation temperature of each kinetic step was reduced by a factor of two. This approach was found to be more robust than adding ignition point sources or linearly scaling the reaction rates. Ignition point sources require that the user specify local energy sources with just enough energy (and at an appropriate location) to ignite the mainstream fuel. If the ignition source is too intense, stability problems can develop. A linear increase of the reaction rates, that is, increasing the preexponential Arrhenius constants, can also degrade numerical stability because this procedure amplifies the nonlinear nature of the reaction rates. Reducing the activation temperature, on the other hand, raises the magnitude of the reaction rates in a manner that reduces the exponential dependence on temperature. After ignition had been established, the activation temperatures were set back to their proper values. The final converged coarse grid reacting solutions were used as the initial guess (via linear interpolation) for each successive fine grid solution. Convergence was ascertained by monitoring the global and species mass flow rates, as well as mass-flux weighted one-dimensional variables of interest. A mass-flux weighted variable $\bar{q}$ at a given streamwise station x is defined by

$$\bar{q}(x) = \frac{\int q\rho(\boldsymbol{v} \cdot \boldsymbol{n})\,\mathrm{d}A}{\int \rho(\boldsymbol{v} \cdot \boldsymbol{n})\,\mathrm{d}A} \tag{2}$$

where ρ, $\boldsymbol{v}$, $\boldsymbol{n}$, and $\mathrm{d}A$ are the mixture density, velocity, cell face unit normal, and cell face area. The integration is performed over

all cell faces at a given cross section of the flowpath. When the one-dimensional properties failed to converge to a steady-state value, a time-accurate simulation was performed until a periodic state was established. A steady-state result was then extracted by performing an ensemble average of the flow properties during one period of the oscillation cycle.

Results

The first set of conditions simulated were the conditions given in Table 2 using the Mach 1.8 facility nozzle. This condition was chosen because measurements were available at these conditions for a similar combustor geometry.[2,6] The primary geometrical difference between the original and current configuration is that the original combustor section had multiple divergence angles, whereas the current combustor has a constant divergence angle. The overall area ratio is the same for both configurations. A thorough grid-dependence study was performed at this condition to determine the minimum level of grid resolution required for adequate resolution of the dual-mode flow physics. Finally, rough comparisons with isolator wall pressure measurements were made to determine the appropriateness of chosen values for the turbulent Prandtl and Schmidt numbers.

The influence of grid resolution is considered first. Figure 5 compares the mass-flux weighted total pressure recovery, mixing efficiency, and static temperature on different grid densities. Comparisons are made on four different grid systems. Three of the grids were coarsened in only one coordinate direction to assess the relative importance of grid resolution in each coordinate direction independently. The fourth grid was coarsened in all three coordinate directions. The total pressure recovery was defined as

$$P_0^{\text{rec}} = \frac{\int P_0 \rho(\boldsymbol{v}\cdot\boldsymbol{n})\,\mathrm{d}A}{\int P_0^{\text{ref}} \rho(\boldsymbol{v}\cdot\boldsymbol{n})\,\mathrm{d}A} \tag{3}$$

where the reference total pressure P_0^{ref}, was taken to be the facility nozzle plenum pressure. The mixing efficiency was defined in the manner described by Mao et al.[14]:

$$\eta_m = \frac{\int Y_r \rho(\boldsymbol{v}\cdot\boldsymbol{n})\,\mathrm{d}A}{\int Y \rho(\boldsymbol{v}\cdot\boldsymbol{n})\,\mathrm{d}A} \tag{4}$$

where Y is the fuel mass fraction (for globally fuel lean cases) or the oxidant mass fraction (for globally fuel rich cases). Y_r is defined as the mass fraction of the least available reactant (based on the global equivalence ratio) that would react if complete reaction took place without further mixing, that is,

$$Y_r = \begin{cases} Y, & Y \le Y_s \\ Y_s[(1-Y)/(1-Y_s)], & Y > Y_s \end{cases} \tag{5}$$

The definition of perfect mixing implied by this measure requires that the least available reactant Y be less than or equal to the stoichiometric value Y_s at every point of a given streamwise plane. All simulations were performed at globally stoichiometric or fuel lean conditions; therefore, Y was chosen as the mass fraction of fuel.

The change in slope of the total pressure drop at $x/H \approx -7$ corresponds to the onset of the precombustion shock train. Apart from a shift in the onset of the shock train location, all four grids yielded comparable levels of total pressure loss. The solution was more sensitive to coarsening of the J-direction than the I and K directions. As will be shown later, the precombustion shock train results in a stronger distortion of the side-wall (J-direction) boundary layer than the body and cowl surface boundary layers, which would explain the larger sensitivity to J-direction resolution. The mixing efficiency comparison shows a similar trend. One interesting feature is that the coarsest grid resulted in the lowest mixing efficiency. A cold-flow simulation that is nearly grid resolved will in general yield higher mixing efficiencies as the grid is coarsened due to increased numerical diffusion. The mixing is strongly coupled with the precombustion shock train strength for dual-mode reacting calculations, complicating the prediction of trends as the grid is resolved or coarsened. The mass-flux weighted static temperature distribution also shows a negligible sensitivity to coarsening in the I and K directions. The precombustion shock train is initiated approximately 1.75 duct heights farther downstream (a shift of roughly 20 grid cells) when the grid is coarsened in all three coordinate directions, resulting in a somewhat weaker shock structure and reduced combustion levels farther downstream. Figure 5 again shows the solution is most sensitive to grid resolution in the spanwise J direction.

Previous dual-mode calculations[5] have shown a strong dependence of the solution to the values specified for the turbulent Schmidt and Prandtl numbers. Thus, existing isolator pressure measurements (at three conditions close to the simulated conditions) were used to assess the adequacy of the chosen values of 0.5 for Sc_t and 0.89 for Pr_t. A comparison of the measured and computed (coarsened I-direction grid) pressure distributions are shown in Fig. 6. The measured pressure profiles along the body and cowl surfaces are

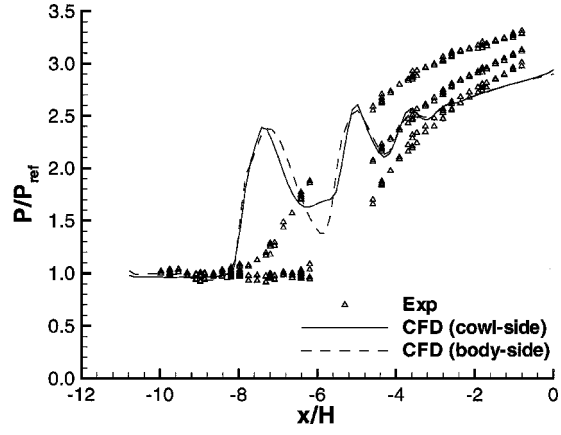

Fig. 6 Comparison of measured and computed isolator pressure distributions.

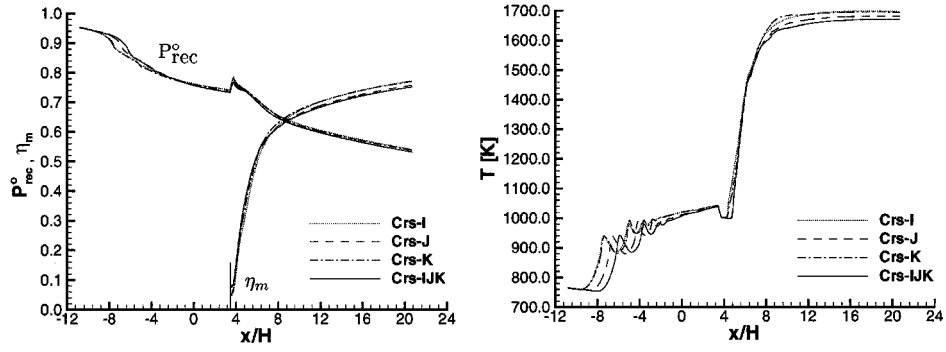

Fig. 5 Sensitivity of mass-flux weighted properties to grid resolution.

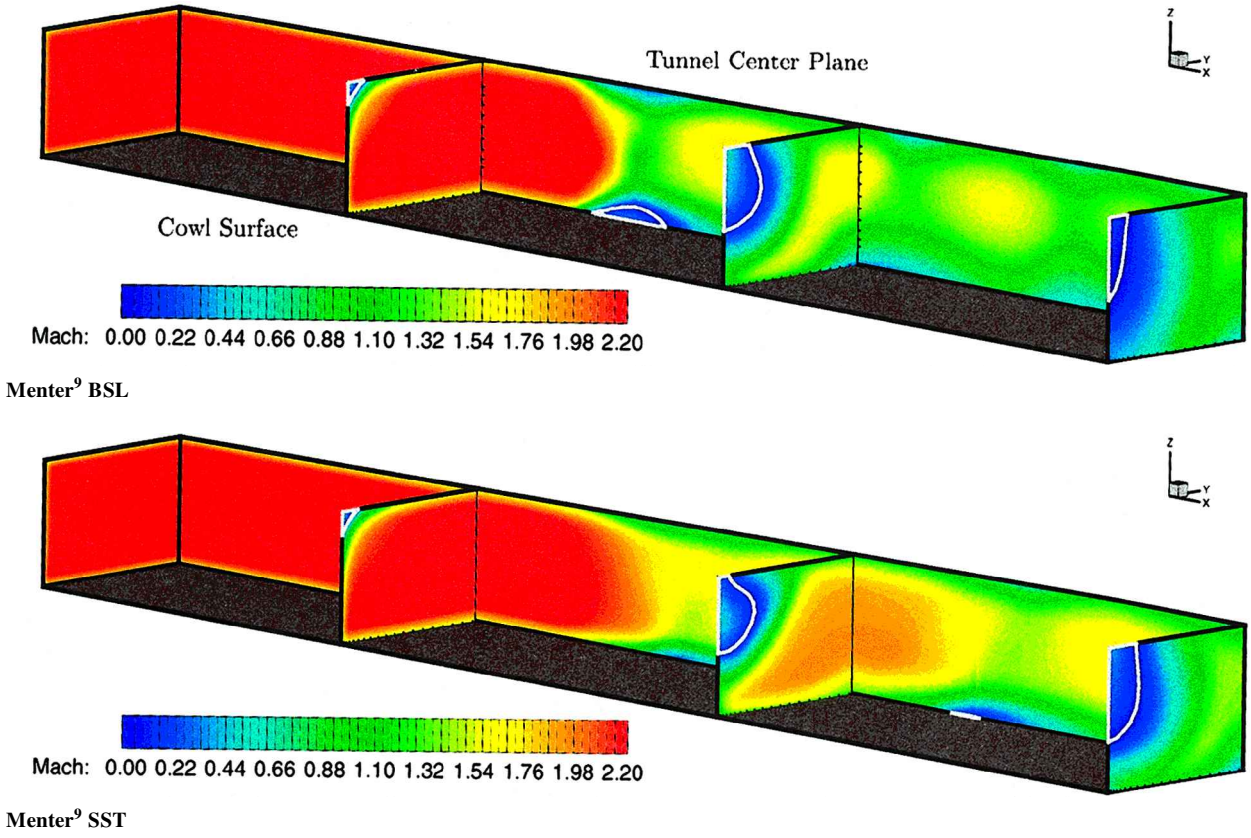

Fig. 7 Isolator Mach contours at the Mach 4.0 flight condition.

practically identical and monotonically increase through the isolator. The computed body and cowl surface pressures are not quite symmetric and show peaks and valleys that result from the complicated three-dimensional precombustion shock structure within the isolator. An increase or decrease of the Schmidt number (reduction or increase of turbulent mixing) tends to shift the shock structure rather than change the three-dimensional nature of the shock train itself. Calculations that neglect the side-wall effects[3] have resulted in monotonic surface pressure distributions similar to that observed in the measurements. This suggests an overprediction of the corner shock influence when the side wall is accounted for, but further research is needed to determine the cause of the discrepancy. Based on the current comparisons, the chosen default values for the turbulent Schmidt and Prandtl numbers appear to be appropriate.

The grid-dependence study performed at the Mach 1.8 combustor entrance condition showed that all of the relevant flow physics were captured with the fully coarsened grid, although some nonnegligible differences were noted. However, as will be shown throughout this paper, the sensitivity of the solution to modeling uncertainties (turbulence model, Schmidt number Sc_t, Prandtl number Pr_t, etc.) overwhelmed the solution sensitivity between the grids employed. Thus, only one set of fine grid results were obtained at each of the remaining flight Mach conditions using the default turbulence model (Menter BSL) and the baseline values chosen for Schmidt number Sc_t and Prandtl number Pr_t. The fully coarsened grid was used for all parametric studies to permit relatively rapid turnaround times.

The Mach 2.2 condition (Table 3) is considered next. Based on estimated levels of OH in the vitiate (less than 0.0025 ppm), the kinetic rates at this condition did not require any adjustments. This condition corresponds to the lowest design flight Mach number (Mach 4.0) considered for the HyTech scramjet propulsion system. The total temperature entering the combustor will never be lower than what is encountered at this flight condition; hence, this case represents the most demanding condition from a flameholding perspective. This condition also drives the isolator length because the total temperature jump due to heat release is a maximum at this condition. The flowfield in the isolator is dominated by shock/boundary-layer interactions, which are notoriously difficult to predict in turbulent flows. The Menter SST model is better suited for certain classes of adverse pressure gradient flows; thus, computations were performed with this model for comparison with results obtained with the Menter BSL model. A steady-state solution could not be found with the SST model; hence all results presented from this simulation were ensemble averaged over one oscillation cycle. The shock movement during one oscillation cycle was on the order of 1–2 duct heights.

The predicted Mach number distribution within the isolator for each turbulence model is shown in Fig. 7. The flow direction in these images (and all other contour images) is from left to right. Regions of streamwise flow separation are outlined with a white contour. These images show that the precombustion shock train initiates at the side-wall/body-side juncture, causing flow separation in the vicinity of the corner on both the side-wall and body surface. Farther downstream, the combustion-induced adverse pressure gradient forms a diamond shock/expansion pattern in the spanwise x–z planes. The expansion process downstream of the initial shocks forces flow back toward the body and cowl surfaces, energizing the boundary layer and discouraging further separation from the initial corner shock along the body-side surface. The spanwise width of the combustor is three times the height; hence, a similar wave structure does not form in the spanwise direction. Without any mechanism present to reenergize the side-wall boundary layer, the separation caused by the incipient corner shock continues to spread along the side wall. As a result, the flow is highly distorted at the combustor entrance.

Both the BSL and SST variants of the Menter[9] turbulence model predict the shock system to initiate at roughly the same location in the isolator, but the shock structure predicted by the SST model is considerably more oblique (weaker) with fewer shock reflections. The SST results, however, show a larger extent of streamwise separation within the low-momentum region. The ramifications of this feature are shown in Fig. 8. The large recirculation zone predicted by the SST model provides a flameholding region in the corner that

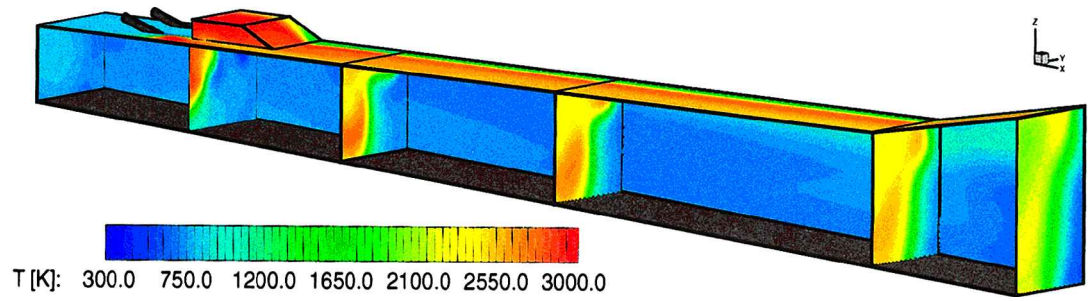

Menter[9] BSL

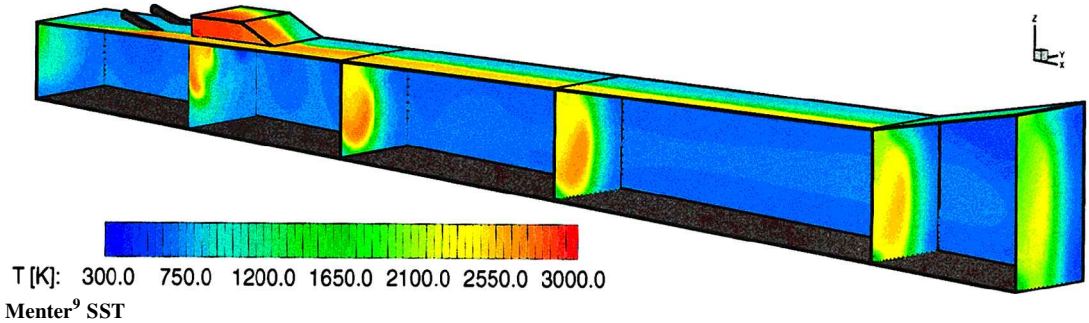

Menter[9] SST

Fig. 8 Combustor temperature contours at the Mach 4.0 flight condition.

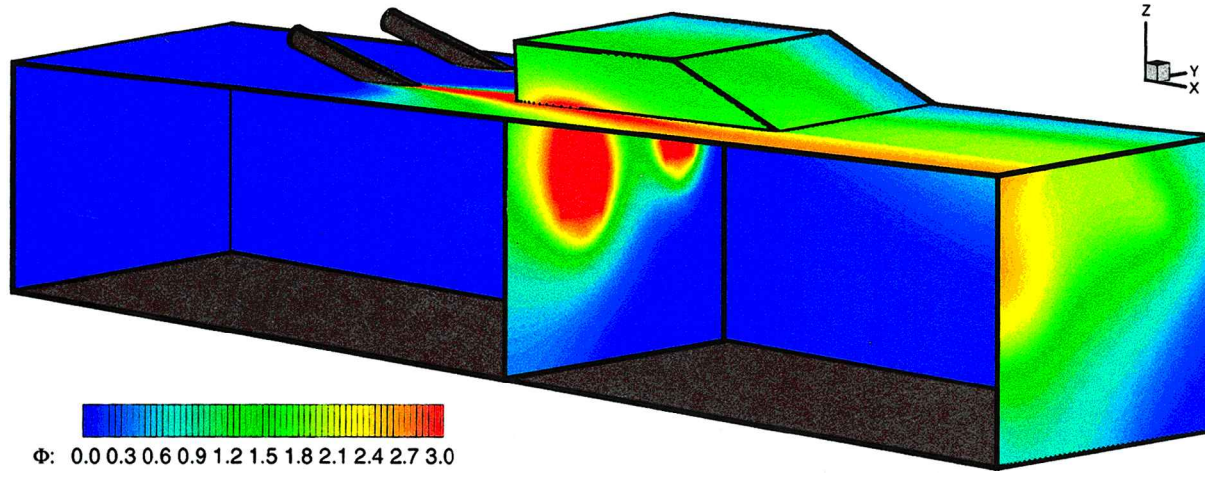

Menter[9] BSL

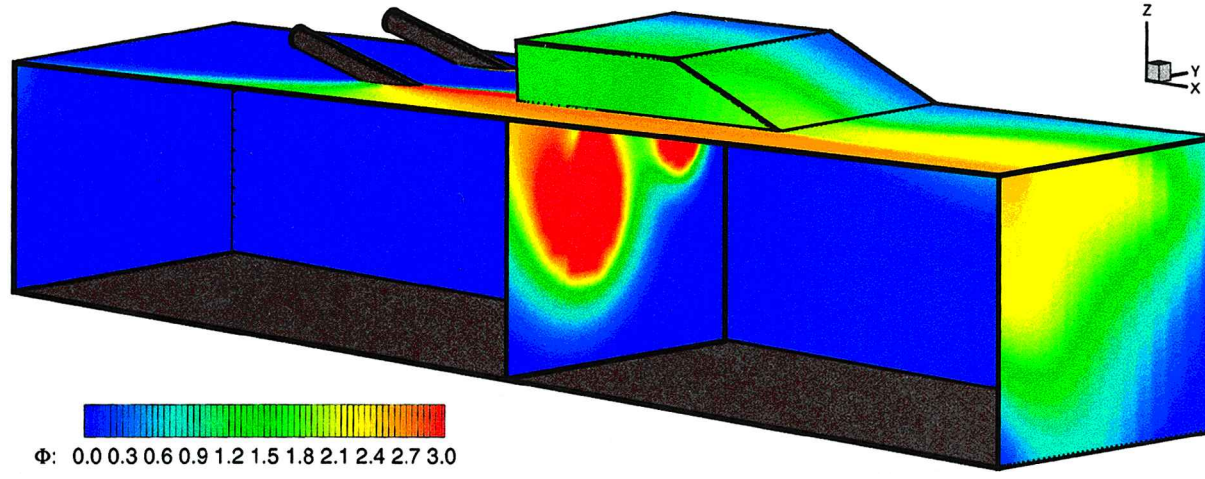

Menter[9] SST

Fig. 9 Combustor equivalence ratio contours at the Mach 4.0 flight condition.

convects hot reaction products well upstream of the fuel injection sites and into the isolator. Both calculations show that the low-momentum region near the corner of the side-wall and body-side surfaces supports combustion, with the flame tending to spread laterally rather than vertically. The pronounced influence of this corner distortion on mixing is clearly seen by examining the equivalence ratio (based on elemental O_2 and C_2H_4) distributions. The equivalence ratio is plotted for the injector near field in Fig. 9. The fuel exiting the injector closest to the side wall spreads much more rapidly into the cavity flameholder and across the duct toward the cowl surface than the fuel plume adjacent to the symmetry plane. This results in a stratification of the flame within the cavity flameholder with poor flame spreading into the core flow near the symmetry plane.

Comparisons between turbulence models of mass-flux weighted properties are considered next. The one-dimensional pressure and Mach distribution (Fig. 10) illustrate the typical trends of dual-mode combustion. The heat release of combustion causes a thermal choke, which forces a shock system upstream into the isolator. The shock train transitions the flow from supersonic to subsonic conditions. The heat release then expands the subsonic flow smoothly to sonic conditions within the divergent duct. The divergent surface of the combustor then continues the expansion process to fully supersonic conditions. The thermal throat based on the mass-flux weighted Mach number occurred at an x/H of 15.5 and 8.5 for the BSL and SST models, respectively. Another interesting point relates to the onset of the precombustion shock train. Both turbulence models predicted the same shock train initiation point with quite different peak pressure rises. This trend can be explained through an understanding of the behavior of each turbulence model. The SST model was designed to encourage flow separation in the presence of an adverse pressure gradient by limiting the eddy viscosity. Thus, for a given level of flow separation, a larger pressure gradient is required when the BSL model is employed. To date, our computational fluid dynamics (CFD) data has consistently underpredicted the peak pressure rise within the isolator when the shock train initiation point is predicted accurately. Based on this observation, the Menter BSL model[9] was chosen as the baseline turbulence model for all remaining parametric evaluations.

The mass-flux weighted static temperature comparisons are given in Fig. 11. The SST model predicts a lower static temperature rise with combustion, as one would expect based on the pressure and Mach distributions shown earlier. The reason for the reduced combustion levels is the lower turbulent mixing levels associated with the SST model. A comparison of the turbulent to molecular viscosity ratio (Fig. 11) shows that the turbulent viscosity coefficient of the SST simulation is roughly two-thirds of that predicted by the BSL model. These lower values also explain why a steady-state solution was not found when the Menter SST model[9] was employed. A full appreciation of the magnitude and extent of the high-viscosity levels associated with these dual-mode simulations can be realized by visualizing the growth of the eddy mass diffusivity ν_t/Sc_t through the precombustion shock train and into the combustor (Fig. 12). The high-viscosity values are initiated at the incipient location of the precombustion shock system (side-wall/body surface corner). The production term of the turbulence kinetic energy equation responds instantaneously to mean shear, rapidly elevating the turbulence kinetic energy (and eddy viscosity) through the interaction of the precombustion shock system with the viscous wall regions. The end result is large-eddy viscosities (orders of magnitude larger than values present in the approach boundary layer) across the entire cross section of the combustor entrance. Note that the combustion process and the precombustion shock train are inherently strongly coupled. Small changes in either the upstream or the downstream conditions can alter the entire flow structure, resulting in a highly unstable flowfield. There exists no direct scaling mechanism within eddy-viscosity-based turbulence models to distinguish between large-scale unsteadiness and unsteady scales associated with the turbulence that are being modeled. Thus, although an unsteady solution was found with the Menter SST model,[9] the eddy viscosity was still quite high. This resulted in what is essentially a bulk (periodic) motion of the shock train from left to right, rather than the more dynamic motion observed during actual combustor operation.

The effect of turbulent Schmidt and Prandtl numbers is considered next. Simulations were performed with the turbulent Prandtl number held fixed at 0.89, and the turbulent Schmidt number offset (increased and decreased) by a factor of 0.25. Similarly, the turbulent Schmidt number was held fixed at 0.5, and the turbulent Prandtl number was increased and decreased by a factor of two. Each simulation employed the Menter BSL turbulence model,[9] with the

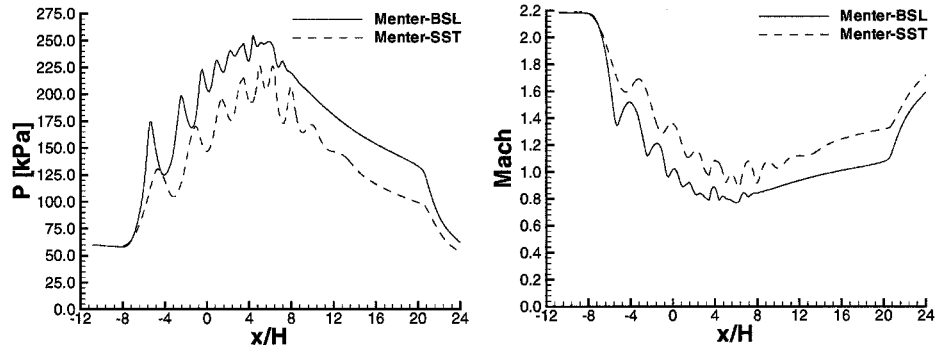

Fig. 10 Mass-flux weighted pressure and Mach number at the Mach 4.0 flight condition.

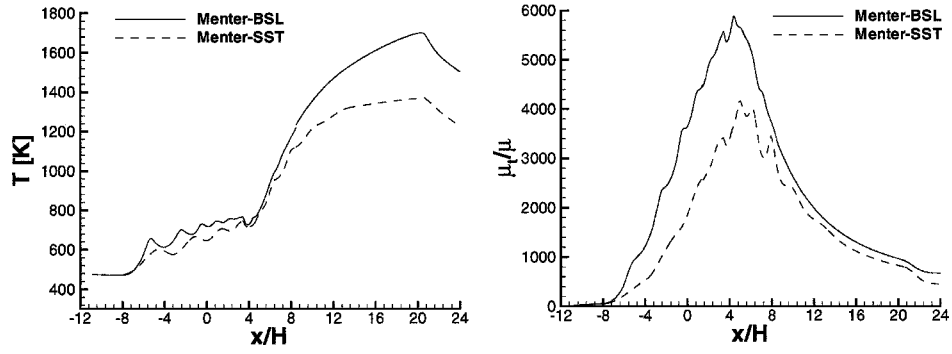

Fig. 11 Mass-flux weighted temperature and eddy to molecular viscosity ratio at the Mach 4.0 flight condition.

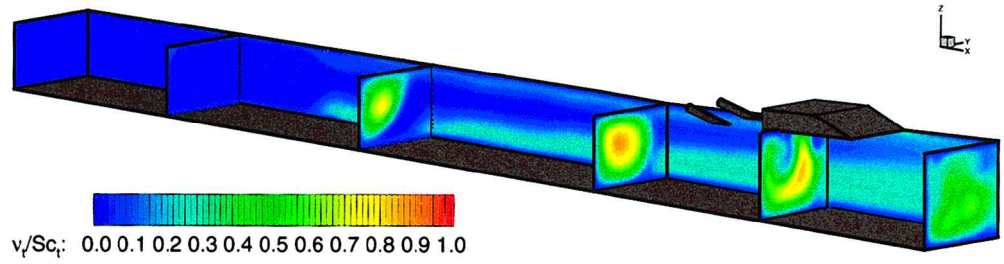

Fig. 12 Isolator/combustor eddy diffusivity (m^2/s) contours at the Mach 4.0 flight condition (Menter BSL).[9]

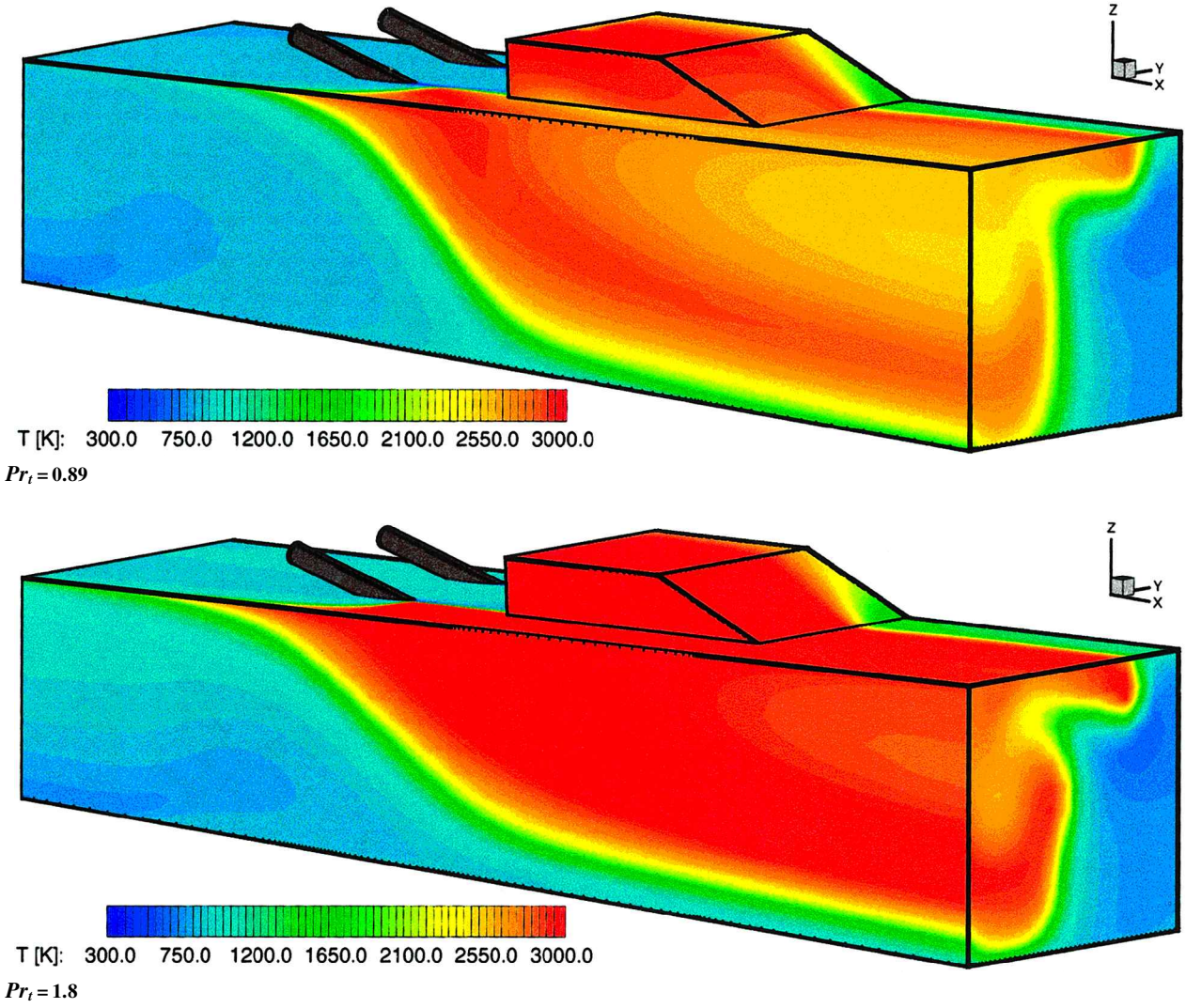

Fig. 13 Combustor surface temperature contours at the Mach 4.0 flight condition.

default Schmidt number Sc_t and Prandtl number Pr_t solution used as the initial condition. A steady-state solution was not found for the reduced turbulent Schmidt number simulation. Thus, an ensemble average was taken over one period of the oscillation cycle. Two of the remaining simulations (reduced Prandtl number and increased Schmidt number) resulted in flame blowout, including the flame within the cavity flameholder. The trend of reduced combustion with increased Schmidt number Sc_t is to be expected because this parameter directly controls the extent of turbulent mixing. The trend of reduced combustion levels with decreased Prandtl number Pr_t is less obvious. One might expect enhanced thermal diffusion to aid in flame spreading, leading to more robust combustion. In some circumstances this scenario is likely to occur. However, at the Mach 4.0 flight condition, flameholding is critical. The enhanced thermal diffusion associated with lowering the turbulent Prandtl number forced too much heat away from the flameholding regions and into the core flow, extinguishing the flame in these regions. This effect is best visualized by comparing the combustor near-field surface temperatures (Fig. 13) at the two turbulent Prandtl numbers that resulted in a stable flame. Note that the combustor walls were assumed adiabatic, so that the heat loss from wall-bounded flameholding regions can only occur along the interface between the core flow and the flameholding zones. As Figs. 13 indicate, the higher turbulent Prandtl number, that is, reduced thermal diffusion, limits the heat exchange between the flameholding zones and the core flow, resulting in a much hotter flame stabilization zone. Turbulent Prandtl numbers as high as 10 were also considered, and the same monotonic trend was observed.

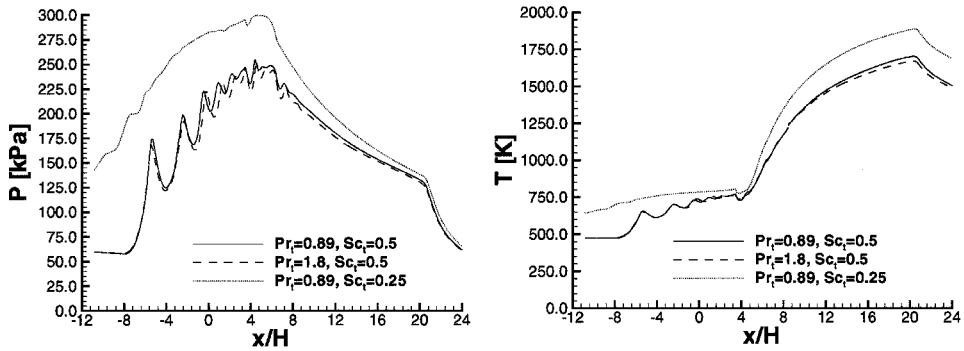

Fig. 14 Sensitivity of mass-flux weighted pressure and temperature at the Mach 4.0 flight condition to variations in Prandtl and Schmidt numbers.

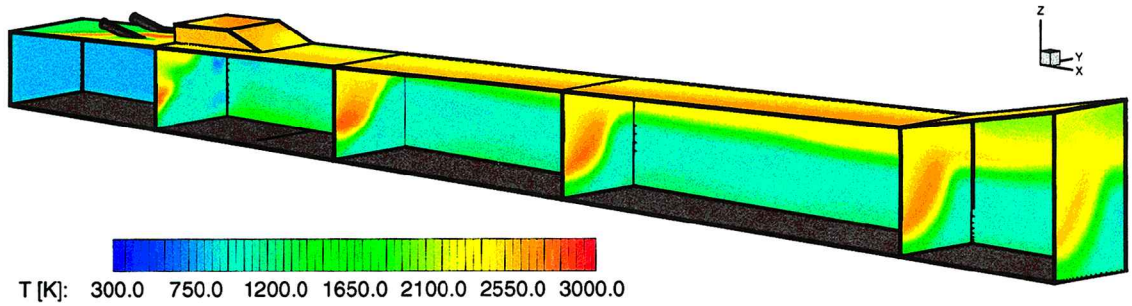

Fig. 15 Combustor temperature contours at the Mach 6.5 flight condition.

The sensitivity of combustor performance to Schmidt number Sc_t and Prandtl number Pr_t variations are shown in Fig. 14. Results from the increased turbulent Schmidt number and reduced turbulent Prandtl number simulations are not shown because combustion was not maintained. The enhanced mixing associated with the reduced turbulent Schmidt number resulted in more intense combustion, which strengthened the precombustion shock train considerably and increased the static temperature rise due to reaction. In fact, the supersonic portion of the facility nozzle had to be included as part of the elliptical domain to hold the resulting shock structure. Note that the pressure rise normalized by the theoretical normal shock pressure rise was approximately 0.8 for each case. The normal shock pressure rise was based on the mass-flux weighted Mach number just upstream of the shock train. The Mach number upstream of the shock train was 1.96 for the reduced Schmidt number Sc_t simulation and 2.18 for the baseline and $Pr_t = 1.8$ simulations. The combustor performance at both Prandtl numbers were similar, with slightly lower static pressure and temperature values noted for the $Pr_t = 1.8$ case. Although the temperature contours of Fig. 13 show higher temperatures in regions of intense combustion when thermal diffusion is inhibited, the largest fraction of mass flow is within the cold-core region of the combustor. Heat release into the core flow is limited with reduced thermal diffusion, resulting in the slightly reduced mass-flux weighted static temperature levels shown in Fig. 14. As a final note, the combustor exit mixing efficiency (not shown) of the $Sc_t = 0.25$ simulation was 7–8% higher than the value obtained with $Sc_t = 0.5$. Increasing the turbulent Prandtl number had a negligible impact on the mixing efficiency.

The Mach 3.0 combustor entrance condition (Table 4) corresponds to a flight Mach number of 6.5. The estimated vitiate OH levels at this condition were on the order of 40 ppm. The Wang and Laskin[13] mechanism predicts roughly a factor of 3 decrease in ignition delay with these levels of OH; thus, the default rates of the reduced model used in this effort (Table 1) were increased by a factor of 3. The combustor at this condition is expected to operate in true scramjet mode (fully supersonic flow throughout the combustor) or in a very weak dual mode. The total temperature at the combustor entrance is relatively high at this condition, resulting in a static temperature that is nearly high enough to support reaction, provided that the fuel and air are adequately mixed. The flow velocity is also higher at this condition (particularly in the absence of a precombustion shock train), which limits the flow residence time for efficient fuel and air mixing. Thus, the primary difficulty at this flight condition is centered around achieving sufficiently fast mixing within the supersonic flow environment.

Figure 15 shows a fence plot of the temperature contours at the Mach 6.5 flight condition using the default modeling constants ($Sc_t = 0.5$ and $Pr_t = 0.89$). The flame distribution within the cavity is quite uniform, and in the absence of a strong precombustion shock train, most of the flameholding is established by the recessed cavity. The heat release in the vicinity of the cavity has forced an oblique shock system to anchor near the fuel injection site, which raises the static temperature of the inflow air and enhances the flame propagation. The propagation of the flame is more uniform over the entire spanwise extent of the cavity than what was observed at the Mach 4.0 flight condition. The combustion-induced oblique shock structure has separated the flow near the body surface/side-wall juncture just upstream of the fuel injectors, which aids in anchoring the flame.

Figure 16 shows the mass-flux weighted pressure and temperature distribution at the Mach 6.5 flight conditions for a variety of turbulent Schmidt and Prandtl number combinations. Based on the mass-flux weighted Mach number (not shown), the operation of the combustor at this condition was not dual mode because the Mach number never dropped below one. Although the mass-flux weighted Mach number never dropped below one, an interrogation of the flowfield revealed that the flow was locally subsonic in the combusting regions during the rapid temperature rise (high heat release) section shown in Fig. 16. The pressure rise due to combustion is at the same level seen at the Mach 4.0 condition. However, the total temperature increase resulting from chemical reaction is a smaller fraction of the incoming total temperature. This together with a higher approach Mach number prevents the flow from thermally choking and limits the amount of upstream interaction. The onset of the precombustion pressure rise varies by as much as two duct heights depending on the turbulent Prandtl and Schmidt number combination employed, and the peak pressure (temperature) varies by as much as 50 kPa (240 K). Note that, although this variation is certainly not negligible, the combustor operation has not been fundamentally altered, as

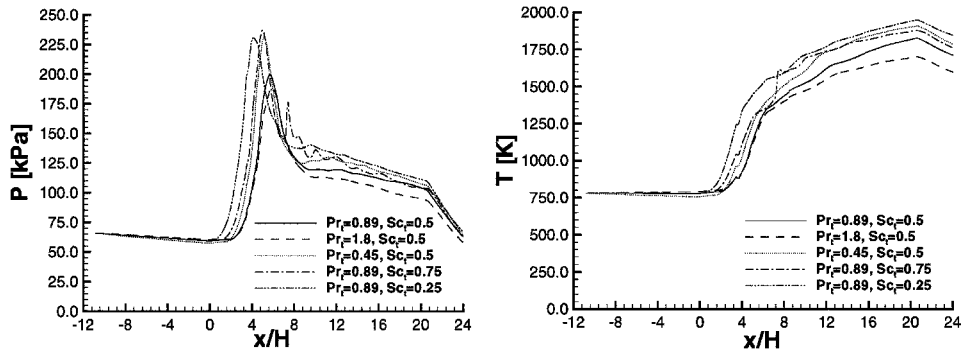

Fig. 16 Sensitivity of mass-flux weighted pressure and temperature at the Mach 6.5 flight condition to variations in Prandtl and Schmidt numbers.

was the case when these parameters were varied at the Mach 4.0 condition.

There are two interesting differences that should be noted when comparing the combustor performance at Mach 4.0 and Mach 6.5 as related to variations in turbulent Prandtl and Schmidt numbers. First the effects of varying turbulent Prandtl number are considered Fig. 16 shows that combustion was enhanced as the turbulent Prandtl number was reduced at the Mach 6.5 condition. Data extracted at the Mach 4.0 condition with the turbulent Prandtl number set to 0.45 showed complete flame blowout, a result caused by heat diffusing out of the flameholding regions at a rate that could not be sustained. At Mach 6.5, combustion of the core flow fuel/air mixture does not require as much flameholding support as that required at the colder Mach 4.0 condition. At the Mach 6.5 condition, enhancement of thermal diffusion allowed heat to be transferred more efficiently through the combustor without starving the flameholding regions. The second observation is that the combustor performance did not vary monotonically with turbulent Schmidt number at the Mach 6.5 condition. Lower turbulent Schmidt numbers imply enhanced species diffusion rates; thus, one would expect more efficient combustion (due to better mixing) as the turbulent Schmidt number is reduced. Figure 16, however, shows a higher peak pressure and temperature when Sc_t was increased from 0.5 to 0.75. No plausible explanation was found for this behavior, which prompted the consideration of a hysteresis effect. The converged baseline reacting solution ($Pr_t = 0.89$ and $Sc_t = 0.5$) was used as the initial condition for all solutions involving variations of turbulent Prandtl and Schmidt numbers. To determine the influence of the path taken to a converged steady-state solution, a solution was obtained with a turbulent Schmidt number of 0.5, but with the initial condition taken as the final converged $Sc_t = 0.75$ solution. The result was compared (Fig. 17) with the original $Sc_t = 0.5$ solution that was obtained using the ignition process outlined earlier. The difference in the final converged solutions indeed points to a hysteresis effect. This effect occurs due to the formation of recirculation (flameholding) zones that form as the solution is integrated in time. Different solution paths, in general, develop different recirculation zones, which in the current situation implies a different distribution of hot flameholding zones. Once these zones develop, they influence the path taken in the temporal integration of the governing equations. Note that this behavior has also been observed in some of our simulations of nonreacting, backpressured internal flows. Similar path-dependent effects have been noted by other similar works as well.[15]

The mixing efficiency and two measures of the combustion efficiency at both the Mach 4.0 and Mach 6.5 conditions ($Pr_t = 0.89$ and $Sc_t = 0.5$) are shown in Fig. 18. These results were extracted from solutions that were initialized in a similar fashion. The first measure of combustion efficiency is simply a measure of the level of fuel decomposition:

$$\eta_{c_1} = \frac{\dot{m}_F^{\text{ref}} - \dot{m}_F}{\dot{m}_F^{\text{ref}}} \tag{6}$$

where the reference fuel mass flow rate is taken to be the total mass flow rate of the fuel injected into the combustor. This measure is not an accurate representation of the efficiency of the chemical processes, but it is a good indicator of whether or not the fuel is being well mixed in regions where the temperature is high enough to support reaction. The second measure of combustion efficiency compares the mass-flux weighted total temperature at a given streamwise station with some ideal value, that is,

$$\eta_{c_2} = \frac{T_0 - T_0^{\text{ref}}}{T_0^{\text{ideal}} - T_0^{\text{ref}}} \tag{7}$$

In this effort, the reference total temperature was taken to be the mass-flux weighted total temperature entering the isolator, and the ideal total temperature was defined as the total temperature that would be achieved at a given streamwise station if the reactions were allowed to reach equilibrium. The equilibrium state at each streamwise station was based on the mass-flux weighted total enthalpy and total pressure taken from the CFD simulation. This measure of combustion efficiency will always be less than or equal to the measure based on fuel depletion.

The mixing efficiency curves show that roughly 85% of the fuel has been mixed out to stoichiometric proportions or less by the end of the combustor at the Mach 4.0 condition compared with only 65% at the Mach 6.5 condition. This result was expected because the residence time is considerably shorter at the Mach 6.5 condition. The flow distortion caused by the precombustion shock train at the Mach 4.0 condition also tends to enhance the mixing process. The combustion efficiencies, however, are comparable at both flight Mach conditions. The combustor exit values for η_{c_1} and η_{c_2} were 0.74 and 0.65 at the Mach 4.0 condition, compared with 0.78 and 0.62 at the Mach 6.5 condition. This indicates that, for a given level of mixing, a larger fraction of the fuel/air mixture will combust at the higher flight Mach condition. Intuitively, this is the trend one would expect because the incoming total enthalpy (temperature) is higher at the Mach 6.5 condition. However, as shown in Figs. 14 and 16, the precombustion shock system at the Mach 4.0 condition has raised the static temperature to a level close to that of the Mach 6.5 core flow. A comparison of the temperature distribution

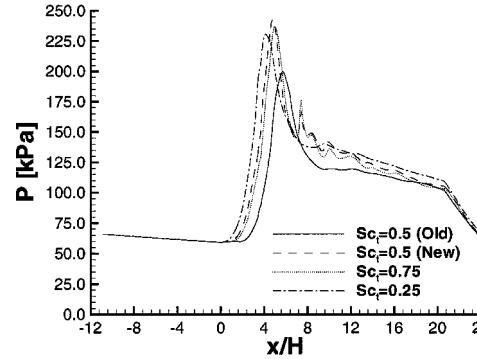

Fig. 17 Sensitivity of mass-flux weighted pressure at the Mach 6.5 flight condition to variations in initial condition.

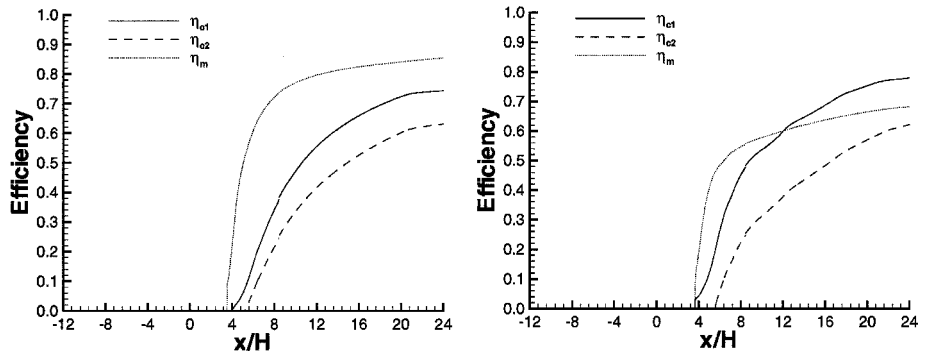

Fig. 18 Mass-flux weighted efficiencies at flight conditions of a) Mach 4.0 and b) Mach 6.5.

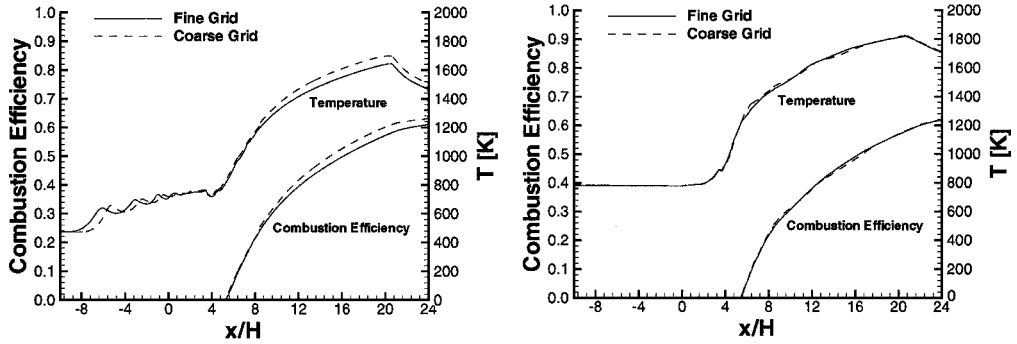

Fig. 19 Sensitivity of mass-flux weighted mixing efficiency and temperature to grid resolution: a) Mach 4.0 and b) Mach 6.5.

(Figs. 8 and 15) is required to explain the enhanced combustion process at the Mach 6.5 condition. The flame at the Mach 4.0 condition is anchored near the side wall of the combustor, providing a flameholding source for the fuel plume closest to the side wall. The combustion of the fuel plume near the symmetry plane was delayed because this fuel, although reasonably well mixed, has little contact with hot gases until the side-wall fuel plume is fully ignited. Also, whereas the core flow temperature upstream of injection at the Mach 6.5 condition was similar to that of the Mach 4.0 condition, the adiabatic surface temperature was considerably higher, uniformly heating the fuel/air mixture in the approach boundary layer upstream of the cavity flameholder. Moreover, the heat release due to combustion at the Mach 6.5 condition forms an oblique shock wave near the fuel injection point, elevating the core flow temperature downstream of injection. As a result, higher static temperatures are present in the core flow in the vicinity of the cavity flameholder, allowing both fuel plumes to ignite once the fuel and air are sufficiently mixed. Although not shown, the rate of total pressure loss in regions of high heat release was significantly larger at the Mach 6.5 condition due to Rayleigh losses that scale with the square of Mach number. The total pressure recovery at the exit of the combustor was 0.39 and 0.24 for the Mach 4.0 and Mach 6.5 conditions, respectively.

Additional simulations were performed at both the Mach 4.0 and Mach 6.5 conditions using the baseline turbulence modeling parameters (Menter BSL model[9] with $Sc_t = 0.5$ and $Pr_t = 0.89$) using the fine grid, which contains twice as many grid cells in each coordinate direction (factor of eight increase in grid density). The mass-flux weighted static temperature and combustion efficiency η_{c_2} distributions obtained from both grids are shown in Fig. 19. The solution variation with grid density at the Mach 4.0 flight condition is quite similar to what was observed for the dual-mode calculations using the Mach 1.8 facility nozzle (Fig. 5). The shock train forms approximately one duct height farther downstream on the coarse grid, and the combustor exit temperature and combustion efficiency differ by approximately 3%. The grid convergence observed at the Mach 6.5 condition is considerably more favorable. The combustor exit temperature and combustion efficiency at this condition differ by only 0.3%.

Conclusions

Reynolds averaged Navier–Stokes calculations have been completed for an AFRL/PRA scramjet combustor designed for Mach 4.0–6.5 flight. Initial calculations were performed at conditions that closely matched those used in previous tests of a similar combustor configuration. These calculations were used to determine approximate values for the turbulent Schmidt and Prandtl numbers for use in the pretest calculations that were performed at the minimum (Mach 4.0) and maximum (Mach 6.5) flight design conditions. The combustor operated in dual mode as expected at the Mach 4.0 condition. The precombustion shock train at this condition formed a large region of low-momentum/separated flow near the combustor side wall. This proved to be a primary source for flameholding with the recessed cavity adding additional flameholding support. The flame propagation at this condition spread laterally from the combustor side wall. These solutions were extremely sensitive to the modeled levels of turbulent mass and heat transfer. Turbulent Schmidt number variations between 0.25 and 0.75 resulted in solutions that covered the entire spectrum from flame blowout to combustor unstart. Clearly this sensitivity is unsettling, placing severe limits on the predictive capabilities of CFD models currently used to simulate these flows. The higher inflow total temperature (and Mach number) associated with the Mach 6.5 condition limited the extent of upstream interaction at this condition. The temperature in the approach boundary layer was considerably higher at this flight condition, resulting in more efficient flame spreading from the recessed cavity into the core flow. The mixing process at the Mach 4.0 flight condition was more efficient than that seen at the Mach 6.5 condition, due primarily to the shock-induced flow distortion and larger residence time. Even with the reduced mixing levels predicted at the Mach 6.5 condition, the combustion efficiency was comparable to that achieved at the Mach 4.0 condition. The grid-resolution study performed in this effort failed to prove the solutions to be

completely grid resolved. However, the fundamental flow features were not altered with a change in grid density by a factor of eight. Moreover, flowfield variations related to modeling uncertainty were far greater than the variations observed with a substantial change in grid resolution. Finally, the initial condition used for some of the simulations was found to influence the final converged steady-state solution. This disturbing observation is a result of the hysteresis involved with the development of flameholding (recirculation) zones. This may suggest a need for time-accurate advancement of the solution starting from a known preignition state.

Acknowledgements

This study was supported by and performed at Wright–Patterson Air Force Base under Contract F33615-98-C-2816, Douglas Davis Technical Monitor. Additional support included a grant of computer time from the Aeronautical Systems Center Department of Defense High Performance Computing Center.

References

[1]Mercier, R. A., and Ronald, T. M. F., "U.S. Air Force Hypersonic Technology Program," AIAA Paper (Plenary Session), *Proceedings of the AIAA 7th International Spaceplanes and Hypersonics Systems and Technology Conference*, 1996.

[2]Jackson, K. R., Gruber, M. R., Mathur, T., Streby, G., Smith, C., and Billig, F., "Calibration of a Newly Developed Direct-Connect High-Enthalpy Supersonic Combustion Research Facility," AIAA Paper 98-1510, April 1998.

[3]Baurle, R. A., Mathur, T., Gruber, M. R., and Jackson, K. R., "Numerical and Experimental Investigation of a Scramjet Combustor for Hypersonic Missile Applications," AIAA Paper 98-3121, July 1998.

[4]Rodriguez, C. G., White, J. A., and Riggins, D. W., "Three-Dimensional Effects in Modeling of Dual Mode Scramjets," AIAA Paper 2000-3704, July 2000.

[5]Eklund, D. R., Baurle, R. A., and Gruber, M. R., "Computational Study of a Supersonic Combustor Fueled by an Aerodynamic Ramp Injector," AIAA Paper 2001-0379, Jan. 2001.

[6]Mathur, T., Streby, G., Gruber, M., Jackson, K., Donbar, J., Donaldson, W., Jackson, T., Smith, C., and Billig, F., "Supersonic Combustion Experiments with a Cavity-Based Fuel Injector," AIAA Paper 99-2102, June 1999.

[7]White, J. A., and Morisson, J. H., "Pseudotemporal Multigrid Relaxation Scheme for Solving the Parabolized Navier–Stokes Equations," AIAA Paper 99-3360, June 1999.

[8]Edwards, J. R., "A Low Diffusion Flux-Splitting Scheme for Navier–Stokes Calculations," *Computers and Fluids*, Vol. 26, No. 6, 1997, pp. 635–659.

[9]Menter, F. R., "Zonal Two Equation k–ω Models for Aerodynamic Flows," AIAA Paper 93-2906, 1993.

[10]Wilcox, D. C., "Wall Matching, a Rational Alternative to Wall Functions," AIAA Paper 89-0611, Jan. 1989.

[11]Wilcox, D. C., *Turbulence Modeling for CFD*, 1st ed., DCW Industries La Cañada, California, 1993.

[12]Singh, D. J., and Jachimowski, C. J., "Quasi-global Reaction Model for Ethylene Combustion," *AIAA Journal*, Vol. 32, No. 1, 1994, pp. 213–215.

[13]Wang, H., and Laskin, A., "A Comprehensive Kinetic Model of Ethylene and Acetylene Oxidation at High Temperatures," Progress Report, Princeton/Air Force Office of Scientific Research, Princeton, NJ, Nov. 1998.

[14]Mao, M., Riggins, D. W., and McClinton, C. R., "Numerical Simulation of Transverse Fuel Injection," NASA CR 1089, 1990.

[15]Ungewitter, J. L., and Dash, S. M., "High-Fidelity Design Oriented Scramjet Propulsive Flowpath Analysis," AIAA Paper 2001-3203, July 2001.